Supplementary Information for the article titled "Coupled Electrohydrodynamic Transport in Rough Fractures: A generalized lubrication theory"

Mainendra Kumar Dewangan[1], Uddipta Ghosh[1,2], Tanguy Le Borgne[2], and Yves Méheust[2]

[1] *Discipline of Mechanical Engineering, Indian Institute of Technology Gandhinagar, Palaj - 382355, Gujarat, India*
[2] *Univ. Rennes, CNRS, Géosciences Rennes (UMR6118), 35042 Rennes, France*

The purpose of this supporting information document is to complement the analysis of the main article. We start by providing a derivation of the Poisson-Nernst-Planck-Navier-Stokes (PNPNS) equations from the fundamental principles (§S1). In §S2, we then present asymptotic analytical solutions to the generalized lubrication equations (Eq. (4.13) in §4.2 of the article) for 2D geometries. §S3 compares our results to those reported in the earlier study of Ghosal [1]. In §S4 we provide detailed explanations of the complete 3D numerical simulations presented in the article to assess the validity of the generalized lubrication equations. We then present a comparison between the predictions of the lubrication theory and numerical simulations of the first principle equations for the special cases of flow in 3D (§S5) and 2D (§S6) test geometries. In the latter we also show analytical predictions obtained from the solutions presented in §S2.

S1 Derivation of the PNPNS equations

The Poisson-Nernst-Planck-Navier-Stokes (PNPNS) equations, on which our generalized lubrication theory is based (see Eq. (3.1)) in the main article, are well-established (if not ubiquitous) in the electrohydrodynamic literature. For the sake of the readers from the fracture flow community who would be unfamiliar with the formalisms of electrohydrodynamics, we provide below a brief derivation of the PNPNS equations.

The Stokes equation for steady flow subjected to an electric field $\mathbf{E}'$ reads

$$0 = -\boldsymbol{\nabla}' p' + \eta \boldsymbol{\nabla}'^2 \mathbf{v}' + \rho' \boldsymbol{E}' = -\boldsymbol{\nabla}' p' + \eta \boldsymbol{\nabla}'^2 \mathbf{v}' + \gamma \left(\boldsymbol{\nabla} \cdot \mathbf{E}'\right) \mathbf{E}' \,, \tag{S1}$$

where the last term accounts for the electrical force and ρ', the charge density, has been eliminated by use of Poisson's equation $\boldsymbol{\nabla}' \cdot \mathbf{E}' = \rho'/\gamma$, which relates the electrical field to the charge density.

The Fickian transport of a solution species of charge q, molecular diffusion coefficient D, and concentration c', is expressed by the Nernst-Planck equation, an advection-diffusion equation in the form $\mathbf{v}' \cdot \boldsymbol{\nabla}' c = -\boldsymbol{\nabla}' \cdot (-D \boldsymbol{\nabla}' c' + \nu q c' \mathbf{E}')$ in which the last term between parentheses

is the solute mass flux resulting from the electrostratic force $qc'\mathbf{E}'$. The mobility of the ionic species is $\nu = D/(k_bT)$, so the Nernst-Planck equation is generally written as

$$\mathbf{v}' \cdot \boldsymbol{\nabla}' c = D\nabla'^2 c' - \frac{qD}{k_bT}\boldsymbol{\nabla}' \cdot (c'\mathbf{E}') \ . \tag{S2}$$

In this study we consider, for the sake of simplicity, an electrolyte consisting of monovalent ionic species, i.e. which carry either a charge e (protonic charge), or $-e$. The equations can easily be generalized to multivalent ions if necessary. By writing the transport equation (S2) for both ionic species (i.e., with $q = e$ or $q = -e$), considering Eq. (S1), recalling Poisson's equation, and introducing the electrical potential ψ' from which the electric field derives ($\mathbf{E}' = -\boldsymbol{\nabla}\psi'$), one obtains the PNPNS equations [2–7]:

$$\mathbf{v}' \cdot \boldsymbol{\nabla}' c'_+ = D\nabla'^2 c'_+ + \frac{eD}{k_bT}\boldsymbol{\nabla}' \cdot \left\{c'_+ \boldsymbol{\nabla}'(\psi')\right\} \tag{S3a}$$

$$\mathbf{v}' \cdot \boldsymbol{\nabla}' c'_- = D\nabla'^2 c'_- - \frac{eD}{k_bT}\boldsymbol{\nabla}' \cdot \left\{c'_- \boldsymbol{\nabla}'(\psi')\right\} \tag{S3b}$$

$$\nabla'^2\psi' = -\left(c'_+ - c'_-\right)/\gamma \tag{S3c}$$

$$0 = -\boldsymbol{\nabla}' p' + \eta\boldsymbol{\nabla}'^2\mathbf{v}' + \epsilon\nabla'^2\psi'\boldsymbol{\nabla}'\psi'; \qquad \nabla' \cdot \mathbf{v}' = 0 \ , \tag{S3d}$$

where $c'_\pm$ are respectively the concentrations of the positive and negative ions.

S2 Asymptotic solutions to the generalized lubrication equations for the special case of 2D geometries

Recall that the generalized lubrication equations, as given in Eq. (4.13) of the main article are given by:

$$\boldsymbol{\nabla}_{\mathrm{H}} \cdot (Q_p \boldsymbol{\nabla}_{\mathrm{H}} p_0) + \boldsymbol{\nabla}_{\mathrm{H}} \cdot (Q_{\mathrm{c}} \boldsymbol{\nabla}_{\mathrm{H}} \tilde{c}) + \boldsymbol{\nabla}_{\mathrm{H}} \cdot (Q_e \boldsymbol{\nabla}_{\mathrm{H}} \phi) = 0 \tag{S4a}$$

$$\boldsymbol{\nabla}_{\mathrm{H}} \cdot (I_p \boldsymbol{\nabla}_{\mathrm{H}} p_0) + \boldsymbol{\nabla}_{\mathrm{H}} \cdot (I_{\mathrm{c}} \boldsymbol{\nabla}_{\mathrm{H}} \tilde{c}) + \boldsymbol{\nabla}_{\mathrm{H}} \cdot (I_e \boldsymbol{\nabla}_{\mathrm{H}} \phi) = 0 \tag{S4b}$$

$$\boldsymbol{\nabla}_{\mathrm{H}} \cdot (J_p \boldsymbol{\nabla}_{\mathrm{H}} p_0) + \boldsymbol{\nabla}_{\mathrm{H}} \cdot (J_{\mathrm{c}} \boldsymbol{\nabla}_{\mathrm{H}} \tilde{c}) + \boldsymbol{\nabla}_{\mathrm{H}} \cdot (J_e \boldsymbol{\nabla}_{\mathrm{H}} \phi) = 0 \tag{S4c}$$

In a 2D geometry, the flow only takes place along the x-direction and hence the y-axis becomes irrelevant. Therefore, the $\boldsymbol{\nabla}_{\mathrm{H}}$ operator effectively becomes, $\boldsymbol{\nabla}_{\mathrm{H}} = \hat{\mathbf{e}}_x \frac{d}{dx}$. The above equations are subject to the following boundary conditions at the two ends of the flow passage (see eqns. (4.14) in the article):

$$\text{At} \quad x = 0, \quad p_0 = p_{\mathrm{in}} - \alpha\kappa^2; \quad \tilde{c} = 1; \quad \phi = 0 \tag{S5a}$$

$$\text{At} \quad x = L_x, \quad p_0 = p_{\mathrm{ex}} - \alpha\kappa^2\tilde{c}_{\mathrm{ex}}; \quad \tilde{c} = c_{\mathrm{ex}}; \quad \phi = -\beta L \tag{S5b}$$

Approximate asymptotic solutions to the local conservation equations can be derived for flow through 2D geometries which are invariant along the y direction (i.e., a only depends on x), and for low surface charge densities, corresponding to low values of zeta potential. To this end, we may assume that $\zeta_{\mathrm{t}} \sim \zeta_{\mathrm{b}} \sim \mathcal{O}(\zeta_0) \ll 1$, which results in electrokinetics in the Debye-Huckel linearization regime [8–10]. In other words, we assume, $e\zeta'_0/kT \ll 1$, implying that the surface potentials are far weaker than the thermal potential. For algebraic simplicity we assume that $h_{\mathrm{t}}(x) = -h_{\mathrm{b}}(x) = h(x)$ and $\zeta_{\mathrm{t}}(x) = \zeta_{\mathrm{b}}(x) = \zeta_0\zeta(x)$, where $\zeta_0 \ll 1$ is the characteristic magnitude of the surface potential (zeta potential). The length of the fracture (or, channel) is taken as $L_x = L$, while L_y can take any value. Essentially such simplifications

lead to a symmetric pore geometry with symmetric charge distribution on the walls. Although this analysis is not directly applicable to real fractures, it nevertheless gives us valuable insight into the phenomena through closed form solutions, which explicitly demonstrate the variations in the related quantities (pressure, concentration etc.) along a 2D conduit. With the foregoing conditions, we can expand all the relevant variables (like, p_0, $\tilde{c}$, ϕ, $u, ...$ etc.) in an asymptotic series of ζ_0 as follows:

$$\chi(x) = \chi_0(x) + \zeta_0\chi_1(x) + \zeta_0^2\chi_2(x) + ... \quad . \tag{S6}$$

The above expansion can be enforced in 2D versions of the local conservation equations (S4a) - (S4c) to deduce asymptotic solutions for pressure, concentration and potential (imposed) distribution in the pore. We only attempt to deduce the first two terms of the asymptotic expansion, namely until $\mathcal{O}(\zeta_0)$.

S2.1 The leading order solutions

We first note from (4.7b) - (4.7d) of the article that the leading order velocity components in ζ_0 are given by:

$$\bar{u}_p^{(0)} = \frac{1}{2}\left(z^2 - \frac{a^2}{4}\right) \qquad \bar{u}_{\rm c}^{(0)} = \alpha\kappa^2\bar{u}_p^{(0)} \qquad \bar{u}_e^{(0)} = 0 \quad . \tag{S7}$$

On the other hand, from Eq. (4.4) and (4.5), subject to (4.3b) of the article, the leading order charge density, EDL potential and salt concentration are simply given by:

$$\rho_0 = 0 \qquad c_0 = 2\tilde{c}_0 \qquad \varphi_0 = 0 \quad . \tag{S8}$$

With the above leading order variables, we can evaluate the leading order flux coefficients required for (S4a) - (S4c) (i.e., Q_p, I_p, $Q_{\rm c}$, $I_{\rm c}, ...$ etc.) from (4.9) - (4.11) of the main article. These are given by: $Q_p^{(0)} = -a^3/12$; $Q_{\rm c}^{(0)} = \alpha\kappa^2 Q_p^{(0)}$; $Q_e^{(0)} = I_p^{(0)} = I_{\rm c}^{(0)} = J_e^{(0)} = 0$; $I_e^{(0)} = -2Pe^{-1}\tilde{c}_0 a$;$J_p^{(0)} = 2\tilde{c}_0 Q_p^{(0)}$; $J_{\rm c}^{(0)} = 2\tilde{c}_0 Q_{\rm c}^{(0)} - 2Pe^{-1}a$. The above expressions can be inserted in equations (S4) to deduce the leading order equations for pressure, concentration and potential distribution along the pore. The said equations have the following form:

$$\frac{d}{dx}\left(Q_p^{(0)}\frac{dp_0^{(0)}}{dx}\right) + \frac{d}{dx}\left(Q_{\rm c}^{(0)}\frac{d\tilde{c}_0}{dx}\right) = 0 \tag{S9a}$$

$$\frac{d}{dx}\left(\tilde{c}_0 a\frac{d\phi_0}{dx}\right) = 0 \tag{S9b}$$

$$\frac{d}{dx}\left(J_p^{(0)}\frac{dp_0^{(0)}}{dx}\right) + \frac{d}{dx}\left(J_{\rm c}^{(0)}\frac{d\tilde{c}_0}{dx}\right) = 0 \quad , \tag{S9c}$$

which is subjected to the following boundary conditions: at $x = 0$, $p_0^{(0)} = p_{\rm in} - \alpha\kappa^2$; $\tilde{c}_0 = 1$; $\phi_0 = 0$ and at $x = L$, $p_0^{(0)} = p_{\rm ex} - \alpha\kappa^2 c_{\rm ex}$; $\tilde{c}_0 = \tilde{c}_{\rm ex}$; $\phi_0 = -\beta L$ (see the conditions (S5a) - (S5b)). It is possible to solve (S9a) - (S9c), subject to the foregoing boundary conditions. The solutions are as follows:

$$\tilde{c}_0 = \ell_4 + (1 - \ell_4)\exp\left\{-\frac{2Pe\ell_1}{3}\int_0^x \frac{d\tilde{x}}{a(\tilde{x})}\right\} \tag{S10a}$$

$$p_0^{(0)} = -\alpha\kappa^2\tilde{c}_0 + 8\ell_1\int_0^x \frac{1}{a^3(\tilde{x})}d\tilde{x} + \ell_2 \tag{S10b}$$

$$\phi_0 = \ell_3\int_0^x \frac{2}{\tilde{c}_0(\tilde{x})a(\tilde{x})}d\tilde{x} \tag{S10c}$$

In the above, the various constants are given by: $\ell_1 = \mathscr{L}_1^{-1}\left(p_{\rm in} - p_{\rm ex}\right)$; $\ell_2 = p_{\rm in}$; $\ell_3 = -\beta L/\mathscr{L}_3$ and $\ell_4 = \left(c_{\rm ex} - \mathscr{L}_2\right)/\left(1 - \mathscr{L}_2\right)$;. Here, we have further defined: $\mathscr{L}_1 = \int_0^L 8a^{-3}dx$; $\mathscr{L}_2 = \exp\left(-2Pe(\ell_1/3)\int_0^L a^{-1}dx\right)$ and $\mathscr{L}_3 = 2\int_0^L \left(\tilde{c}_0 a\right)^{-1}dx$.

There are several interesting points to note from the leading order analytical solutions. Firstly, at leading order, the electroosmotic flow does not contribute to the pressure (p_0) and the bulk concentration ($\tilde{c}$) along the pore. Both pressure and the bulk concentration (at leading order) solely depend on the geometric shape of the pore walls, as evident from the above relations. We further note that the concentration distribution is not linear; rather it varies exponentially along the conduit. Such variations ensure that the advective transport of dissolved salt is balanced by its diffusive transport, in steady state. The above relations also reveal that at leading order, the externally imposed potential is independent of any flow and is only influenced by the pore shape and the bulk concentration distribution. A quick look at (S10c) tells us that the potential is basically governed by the requirement of conservation of the conduction current carried by the ions. Finally, the induced pressure $p_{\rm ind} = p_0 - (p_{\rm in} - p_{\rm ex})(x/L_x)$ strongly depends on the bulk concentration distribution and the conduit geometry, as expected from Eq. (4.6) of the main article.

Further simplifications are possible for particular choices of $a(x)$ and $c_{\rm ex}$. As a first example, we analyze the case with $c_{\rm ex} = 1$, i.e., for a scenario where no imposed concentration gradients are present. It can be easily shown that this leads to $\tilde{c}_0 = 1$ everywhere in the pore, indicating absence of any concentration polarization in the leading order of ζ_0. As a second example, we can consider a case of uniform pore height ($a(x) = 1$), without imposing $c_{\rm ex} = 1$. Such a physical scenario will result in $\tilde{c}_0 = \ell_4 + (1 - \ell_4)\exp\left(-2Pe\ell_1 x/3\right)$, which for $2Pe\ell_1/3 \ll 1$ can be approximated as, $\tilde{c}_0 = 1 + (2Pe\ell_1/3)(\ell_4 - 1)x$. Consequently, the pressure reads: $p_0^{(0)} = -\alpha\kappa^2 + \ell_2 + \left(8\ell_1 - \alpha\kappa^2(2Pe\ell_1/3)(\ell_4 - 1)\right)x$, while the potential simply has the solution, $\phi_0 = \frac{\ell_3}{(2Pe\ell_1/3)(\ell_4 - 1)}\log\left(1 + (2Pe\ell_1/3)(\ell_4 - 1)x\right) \approx \ell_3 x$. From a physical point of view, these solutions indicate that for weak flows (when $Pe \ll 1$) and very low surface charge density/potential, the bulk concentration, imposed potential and pressure vary linearly in a conduit with straight walls.

S2.2 The $O(\zeta_0)$ solutions

Based on Eq. (4.4), (4.5) and (4.7b)–(4.7d) in the main article, subjected to boundary conditions (4.3), the pertinent variables (velocity, EDL potential, charge density etc.) are given at order $O(\zeta_0)$ by:

$$\bar{u}_p^{(1)} = \bar{u}_{\rm c}^{(1)} = 0; \;\; \bar{u}_e^{(1)} = \alpha\left(\zeta(x) - \varphi_1\right) \tag{S11a}$$

$$\varphi_1 = \zeta(x)\frac{\cosh\left(\kappa\sqrt{\tilde{c}_0}z\right)}{\cosh\left(\kappa\sqrt{\tilde{c}_0}a/2\right)}; \;\; \rho_1 = -2\tilde{c}_0\varphi_1; \;\; c_1 = 2\tilde{c}_1\ . \tag{S11b}$$

The resulting flux components along the flow passage are given by:

$$Q_p^{(1)} = Q_{\rm c}^{(1)} = 0\ ;\ Q_e^{(1)} = 2\alpha\zeta h\left[1 - \tanh(\omega)/\omega\right]\ ; \tag{S12a}$$

$$I_p^{(1)} = -2\tilde{c}_0\int_{-a/2}^{a/2}\varphi_1\bar{u}_p^{(0)}dz\ ;\ I_{\rm c}^{(1)} = \alpha\kappa^2 I_p^{(1)} + q_1(x)\ ;\ I_e^{(1)} = -2Pe^{-1}\tilde{c}_1 a\ ; \tag{S12b}$$

$$J_e^{(1)} = \tilde{c}_0\left(2Q_e^{(1)} + q_1\right)\ ;\ J_p^{(1)} = 2\tilde{c}_1 Q_p^{(0)}\ ;\ J_{\rm c}^{(1)} = \alpha\kappa^2 J_p^{(1)}\ , \tag{S12c}$$

where we have defined $\omega(x) = \kappa\sqrt{\tilde{c}_0}a/2$ and $q_1(x) = 2Pe^{-1}\int_{-a/2}^{a/2}\varphi_1 dz = 2Pe^{-1}\zeta a\tanh(\omega)/\omega$. Note that the first electrokinetic effects on the overall transport occurs at $\mathcal{O}(\zeta_0)$, for $\zeta_0 \ll 1$,

through two basic mechanisms: (i) occurrence of a charge distribution, which alters the local ion concentrations and (ii) altering of the flow field by generation of an electroosmotic flow. The $\mathcal{O}(\zeta_0)$ equations can be determined from Eq. (S4), by enforcing in it the expansion (S6). These have very similar forms to their leading order counterparts (see Eq. (S9)) and therefore, we do not explicitly mention them here for the sake of brevity. The $\mathcal{O}(\zeta_0)$ equations are subject to the following boundary conditions, at $x = 0$, and at $x = L$, $p_0^{(1)} = 0$; $\tilde{c}_1 = 0$; $\phi_1 = 0$. It is possible to solve the $\mathcal{O}(\zeta_0)$ equations to deduce the first order corrections to the pressure, bulk concentration and potential (imposed) distribution along the axis of the channel. The solutions are as follows:

$$\tilde{c}_1 = \exp\left(-\frac{2Pe\ell_1}{3}\int_0^x \frac{d\tilde{x}}{a(\tilde{x})}\right)\left[\int_0^x q_2(\tilde{x})\exp\left(\frac{2Pe\ell_1}{3}\int_0^{\tilde{x}}\frac{dt}{a(t)}\right)d\tilde{x} + \ell_7\int_0^x \frac{2}{a(\tilde{x})}\exp\left(\frac{2Pe\ell_1}{3}\int_0^{\tilde{x}}\frac{dt}{a(t)}\right)d\tilde{x}\right] \tag{S13a}$$

$$p_0^{(1)} = \alpha\kappa^2\tilde{c}_1 + \int_0^x\left[\frac{24\alpha\zeta(\tilde{x})\ell_3}{\tilde{c}_0 a^3(\tilde{x})}\left(1-\frac{\tanh(\omega)}{\omega}\right)+\frac{2\ell_5}{a(\tilde{x})}\right]d\tilde{x} \tag{S13b}$$

$$\phi_1 = \int_0^x\left[\frac{4Pe\ell_1 I_p^{(1)}(\tilde{x})}{\tilde{c}_0 a^4(\tilde{x})}+\frac{2Pe\ell_1\zeta(\tilde{x})\left(\ell_4-\tilde{c}_0\right)}{3\tilde{c}_0 a(\tilde{x})}\left(\frac{\tanh\omega}{\omega}\right)-\frac{2\tilde{c}_1\ell_3}{\tilde{c}_0(\tilde{x})^2 a(\tilde{x})}+\frac{2\ell_6}{\tilde{c}_0(\tilde{x})a(\tilde{x})}\right]d\tilde{x}, \tag{S13c}$$

where the various constants and functions are defined as follows:

$$\ell_5 = -\mathscr{L}_4/\mathscr{L}_1\ ;\ \ell_6 = -\mathscr{L}_5/\mathscr{L}_3\ ;\ \ell_7 = -\mathscr{L}_7/\mathscr{L}_6\ ;$$

$$q_2(x) = \frac{Pe\ell_3}{a^2(x)}\left(2Q_e^{(1)}+q_1(x)\right)-\frac{2Pe\tilde{c}_0(x)\ell_5}{3a(x)}-\frac{2\alpha\ell_3 Pe\zeta(x)}{a(x)}\left(1-\frac{\tanh(\omega)}{\omega}\right),$$

with

$$\mathscr{L}_4 = \int_0^L \frac{24\alpha\zeta(x)\ell_3}{\tilde{c}_0 a^3(x)}\left(1-\frac{\tanh(\omega)}{\omega}\right)dx \tag{S15a}$$

$$\mathscr{L}_5 = \int_0^L\left[\frac{4Pe\ell_1 I_p^{(1)}(x)}{\tilde{c}_0 a^4(x)}+\frac{2Pe\ell_1\zeta(x)\left(\ell_4-\tilde{c}_0\right)}{3\tilde{c}_0 a(x)}\left(\frac{\tanh\omega}{\omega}\right)-\frac{2\tilde{c}_1\ell_3}{\tilde{c}_0(x)^2 a(x)}\right]dx \tag{S15b}$$

$$\mathscr{L}_6 = \exp\left(-\frac{2Pe\ell_1}{3}\int_0^L\frac{dx}{a(x)}\right)\int_0^L q_2(x)\left\{\exp\left(\frac{2Pe\ell_1}{3}\int_0^x\frac{dt}{a(t)}\right)\right\}dx \tag{S15c}$$

$$\mathscr{L}_7 = \exp\left(-\frac{2Pe\ell_1}{3}\int_0^L\frac{dx}{a(x)}\right)\int_0^L\frac{2}{a(x)}\left\{\exp\left(\frac{2Pe\ell_1}{3}\int_0^x\frac{dt}{a(t)}\right)\right\}dx \tag{S15d}$$

There are several important points to note from the solutions presented in (S13). First, we note that the variations in pressure (S13b) are strongly dependent on the surface potential (the first term in the integral), while they also depend on the concentration distribution from the previous order. This indicates a coupling between hydrodynamic, electrical and solute transport appearing for the first time at $\mathcal{O}(\zeta_0)$. Of course, the pressure also depends on the fracture geometry. A second important point to note from (S13a) is that $\tilde{c}_1$ is in general non-zero even if there is no imposed concentration gradient along the fracture (i.e., $c_{\text{ex}} = 1$). This indicates that the heterogeneous structure of the wall coupled with the surface charge inherently leads to an induced concentration polarization [7, 11] in the fracture. Since this effect occurs at $\mathcal{O}(\zeta_0)$, the formation of an EDL is necessary for such effects to come about. Finally, we note from (S13c) that the bulk potential is indeed influenced by the flow as well as

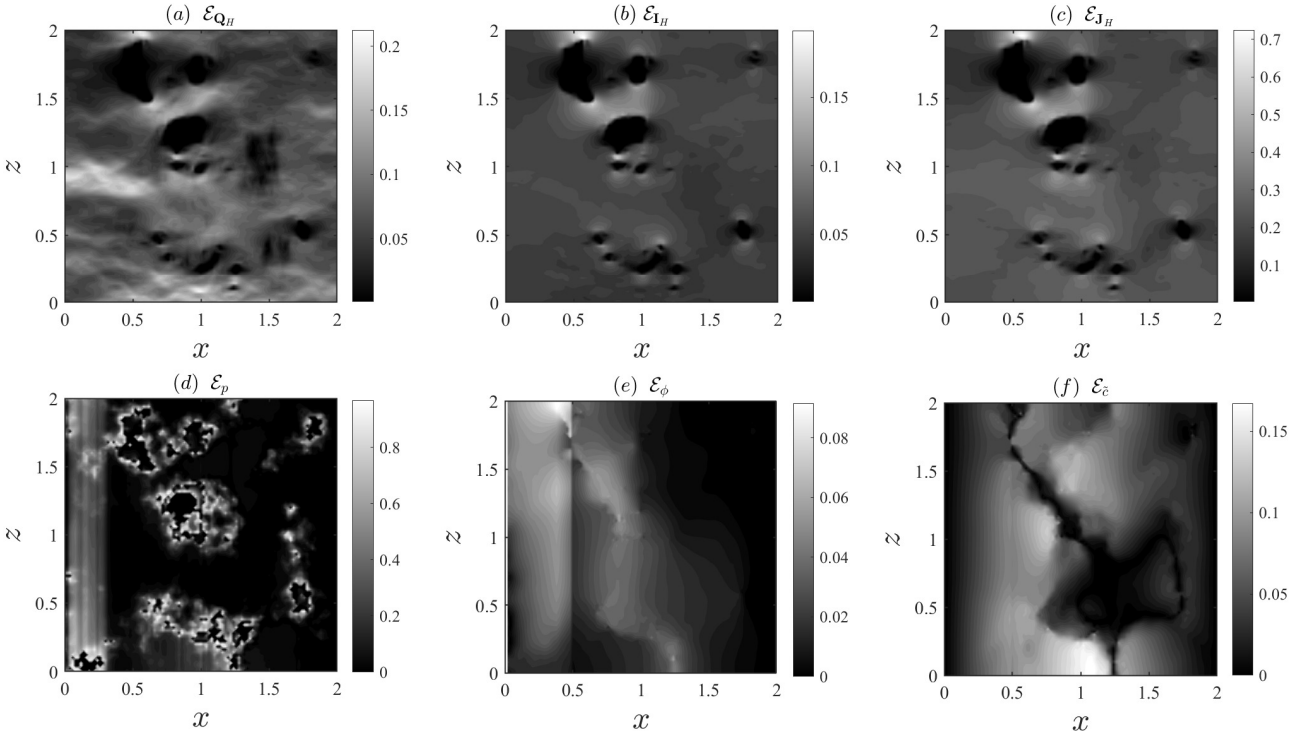

Figure S1: Relative difference ($\mathcal{E}$) between the fluxes and primitive quantities as computed based on the lubrication equations of Ghosal [1] and the generalized equations of the present work, for Realization 2 and $\zeta(x, y) = \zeta_0 = -1.5$, $\kappa = 10$; values of other relevant parameters remain the same as in Table 2 in the article. Panel-wise errors are: Relative errors in (a) fluid mass flux $\mathbf{Q}_\mathrm{H}$, (b) cross-sectional current $\mathbf{I}_\mathrm{H}$, (c) cross-sectional salt flux $\mathbf{J}_\mathrm{H}$, (d) total pressure p, (e) centerline potential ϕ and (f) bulk concentration $\tilde{c}$.

the charge distribution in the fracture at $\mathcal{O}(\zeta_0)$. The dependence on the flow is controlled by Pe, while the dependence on the charge distribution is controlled by $I_p^{(1)}$ as well as ω, which contains information about the local Debye length. At $\mathcal{O}(\zeta_0)$, the potential also shows stronger variations with the fracture geometry. Therefore, in summary, at $\mathcal{O}(\zeta_0)$, the coupling between hydrodynamic, solute and electrical transport becomes apparent. In principle, one can carry on to deduce the higher order solutions in ζ_0 using the same procedure as outlined herein. However, the algebra quickly becomes extremely complicated as we proceed to higher order corrections.

S3 Comparison of the outcome of the generalized lubrication equations to that of Ref. [1]

To directly compare the fluxes computed from the solutions to the generalized equations presented in our study to that of Ghosal [1], we have extended the equations of the latter model (Eq. (4.19) in the article) to configurations for which the fracture geometry, concentrations, pressure and electrical potential depend both on the longitudinal coordinate x and on the transverse in-plane coordinate y. Let us recall here that Eqs. (4.9), (4.11), and (4.12) in the article provide respectively the dependence of the cross-sectional fluid mass, electrical current, and salt fluxes, on the gradients of pressure, solute concentration and electrical potential in the generalized lubrication theory. For a uniform and stationary concentration field ($\tilde{c} = 1$), and

in the thin EDL limit, as considered by Ghosal, these same fluxes boil down to the following :

$$\mathbf{I}_{\mathrm{H}} = -2Pe^{-1}a(x,y)\boldsymbol{\nabla}_{\mathrm{H}}\phi; \;\; \mathbf{J}_{\mathrm{H}} = 2\left(-\frac{a^3}{12}\boldsymbol{\nabla}_{\mathrm{H}}p + \alpha\zeta a\boldsymbol{\nabla}_{\mathrm{H}}\phi\right) \;\text{ and }\; \mathbf{Q}_{\mathrm{H}} = \mathbf{J}_{\mathrm{H}}/2 \; . \tag{S16}$$

Consequently, the potential and the pressure now satisfy the "2D-version" of Eq. (4.19) in the article, i.e.,

$$\boldsymbol{\nabla}_{\mathrm{H}} \cdot \left[-\frac{a^3(x,y)}{12}\boldsymbol{\nabla}_{\mathrm{H}}p + \alpha\zeta(x,y)a(x,y)\boldsymbol{\nabla}_{\mathrm{H}}\phi\right] = 0 \;\text{ and }\; \boldsymbol{\nabla}_{\mathrm{H}} \cdot (a(x,y)\boldsymbol{\nabla}_{\mathrm{H}}\phi) = 0 \; . \tag{S17}$$

One can therefore compute the pressure and potential distribution along with the fluxes based on Eqs (S16) and (S17) for a given realization of the fracture geometry.

We now compare the output from this model to that of our generalized lubrication equations for the fracture geometry denoted "Realization 2" in section 5.2.1 of the article, and for the parameters mentioned in the the caption of Fig. S1. We show the differences between the fluxes and other related quantities as computed using the two sets of equations. To this end, a generic relative difference in any quantity, say Γ, is defined as:

$$\mathcal{E}_{\Gamma} = \frac{\Gamma_{\mathrm{GLT}} - \Gamma_{\mathrm{TEDL}}}{\mathrm{Max}\left(|\Gamma_{\mathrm{GLT}}|\right)} \; , \tag{S18}$$

where Γ_{GLT} is the quantity evaluated from the generalized lubrication theory and Γ_{TEDL} is that same quantity computed using Eqs. (S16) and (S17). Here, Γ may be the pressure (p), the electrical potential (ϕ), the bulk concentration ($\tilde{c}$), or the fluid mass flux ($\mathbf{Q}_{\mathrm{H}}$), etc. For the fluxes, the relative errors are computed based on their magnitudes. Fig. S1 shows the resulting relative difference maps for the three primitives quantities (second row) and three relative fluxes (first row). It appears clearly that the generalized lubrication theory does predict alterations in the fluxes as compared to earlier studies. The most notable change perhaps occurs in panel (c), namely in the salt flux, wherein the differences can be as large as 70%, and in the pressure field, where the discrepancy can reach over 90%. The reason is that Ghosal [1]'s model does not account for the possibility of spontaneous concentration variations required to conserve the salt fluxes – a phenomenon that our model implements. The fluid mass flux (panel (a)) and the current (panel (b)) depict moderate levels of relative differences. The source of these differences may be traced back by comparing the expressions for the fluxes as given in (S16) to those from the generalized lubrication equations. as given in Eqs (4.9), (4.11) and (4.12) in the article. A smaller relative error is however observed in the variations of the potential (panel (d)), which remains below 10% for the particular choices of parameters here.

Finally, it must be noted that the relative differences shown in Fig. S1 are very sensitive to the choices of the zeta potential (ζ_0) and Debye length (κ). For larger values of κ, which more aptly represents the thin EDL limit, the differences are expected to vanish in the absence of imposed concentration gradients. Similar trends are also expected for small values of ζ_0, which represent weakly charged fracture walls.

S4 Details of 3D numerical simulations in rough synthetic fractures

The geometry of the fracture and its aperture field have already been shown in figure 2, §5.1 of the article. Here we discuss how that geometry was generated for carrying out the 3D numerical simulations. The surface topographies of the fracture walls were generated on a 41×41 grid

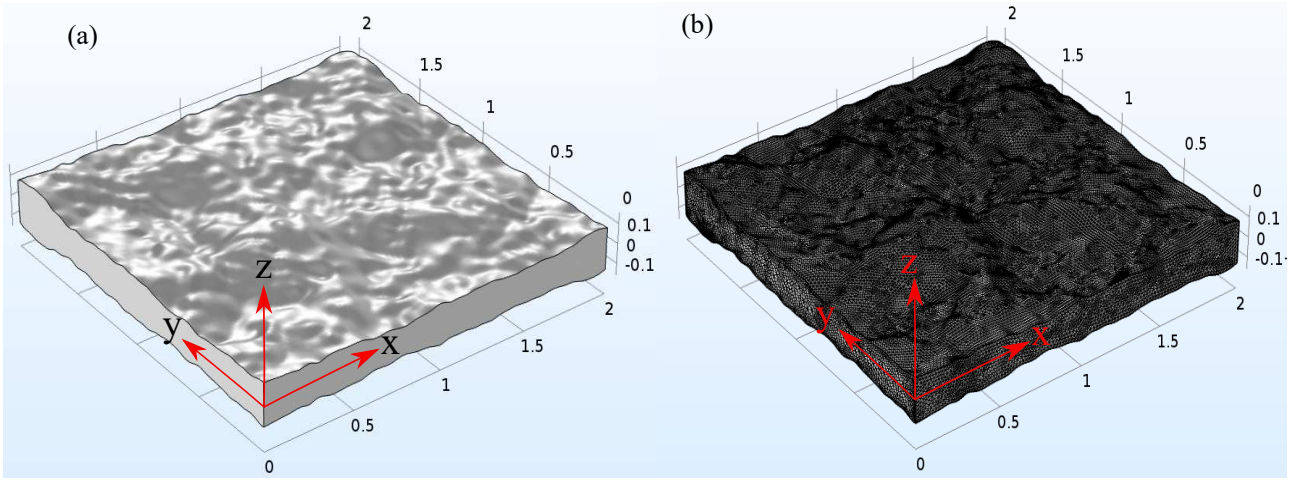

Figure S2: (a) Representative schematic of the 3D computational domain of a synthetic rough fracture for the complete numerical simulations. The fracture has correlation length $L_c = l_0 = 1$, spatial dimensions, $L_x = L_y = 2$, mean aperture $a_{\mathrm{m},*} = \varepsilon = 0.2$ and standard deviation $\sigma_* = 0.2a_{\mathrm{m},*}$. The fracture walls are symmetric in nature with, $h_{\mathrm{t},*} = (1/2)a_*(x_*, y_*)$ and $h_{\mathrm{t},*} = -h_{\mathrm{b},*}(x_*, y_*)$. The surface potential is given by: $\zeta_{\mathrm{b}} = \zeta_{\mathrm{t}} = \zeta_0 \sin(2\pi x_*)$. (b) Mesh created in COMSOL Multiphysics to solve the governing equations.

on the (x_*, y_*) plane, the data for which were exported to the commercially available computer graphics software Dassault Systèmes SolidWorks 2017. The point cloud option in the Solid Works was used with a total of 1681 nodes (41×41), to fabricate the rough surface topography of the fracture. This geometry created in the Solid Works was subsequently exported to COMSOL Multiphysics 5.3, another commercially available finite-element based software, where the 3D numerical simulations were carried out. A representative three-dimensional rendering of the geometry with $a_{\mathrm{m},*} = \varepsilon = 0.2$ and $\sigma_* = 0.2a_{\mathrm{m},*}$ is shown in figure S2(a). The meshing for this geometry is illustrated in panel (b). Recall that the complete 3D numerical simulations were carried out by solving Eq. (3.4) in the article, subjected to boundary conditions (3.5) and (3.6). For other details one may refer to §5.1 of the article.

The MUMPS (Multifrontal Massively Parallel Sparse, see [12, 13]) direct solver with relative tolerance $\tau = 10^{-4}$ was used to obtain the numerical solutions. The computations were carried out for different mean aperture values: $a_{\mathrm{m},*} = \varepsilon = 0.1$, 0.2, and 0.3 with a standard deviation $\sigma_* = 0.2a_{\mathrm{m},*}$. A tetrahedral unstructured mesh was used to discretize the computational domain as depicted in Figure S2(b). The size of the computational cells depends on the maximum and minimum element sizes, element size growth rate, and maximum allowed iterations, which in turn depend on the mean aperture, ε. In addition, the mesh size has to be smaller close to the top and the bottom surfaces, to accurately capture the variations within the EDL. The total number of computational cells were chosen as 1046332, 1576994 and 1684532, for $\varepsilon = 0.1$, 0.2 and 0.3 respectively. We found that further refining the mesh did not affect the accuracy of the simulations. The simulations were carried out in a workstation with 32-core (64 threads) Intel Xeon (R) gold 6130 processors and 256 GB RAM. Relatively large computational times, approximately 14 to 18 hours, were needed to complete each of the simulations, which varied in accordance to the values of ε.

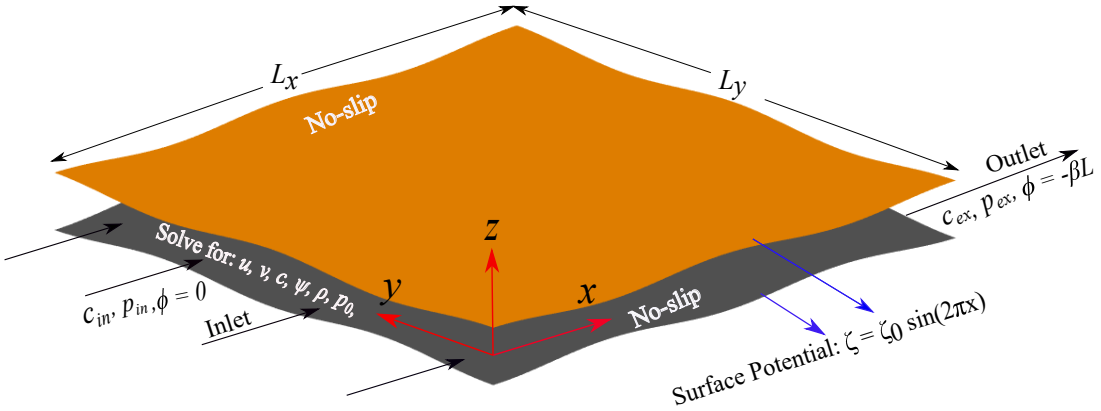

Figure S3: Schematics of the test geometry used to compare the accuracy of the lubrication theory against 3D numerical simulations of the PNPNS equations. The flow passage is located between $H_{\mathrm{t},*}(x_*, y_*)$ (top surface) defined by Eq. (S19) and $H_{\mathrm{b},*}(x_*, y_*) = -H_{\mathrm{t},*}(x_*, y_*)$ (bottom surface). The surface potential is given by: $\zeta_{\mathrm{b}} = \zeta_{\mathrm{t}} = \zeta_0 \sin(2\pi x_*)$. Inlet and outlet conditions remain same as in Eq. (S5).

S5 Comparison of lubrication theory and 3D numerical simulations in a test geometry

S5.1 Description of the test geometry

The 3D test geometry for validating the lubrication theory is shown in Figure S3. The flow passage is symmetric in nature, the top and bottom surface topographies being respectively defined as

$$H_{\mathrm{t},*}(x_*, y_*) = \varepsilon \left[\frac{2}{5} + R \left\{ \cos\left(\frac{4\pi x_*}{L_x} \right) + \cos\left(\frac{4\pi y_*}{L_y} \right) \right\} \right] \tag{S19}$$

and $H_{\mathrm{b},*} = -H_{\mathrm{t},*}$. Recall that the variables with the superscript "$_*$" were introduced in §3 in the article to denote the dimensionless quantities prior to re-scaling. For this validation, we have considered a symmetric surface potential of the form: $\zeta_{\mathrm{t}}(x_*) = \zeta_{\mathrm{b}}(x_*) = \zeta(x_*) = \zeta_0 \sin(2\pi x_*)$; this particular choice of surface charge results in faster convergence of the 3D numerical simulations, without loss of generality with respect to the model validation.

We compare the same quantities between the lubrication theory and 3D numerical simulations as considered in §5.1 of the article. These quantities are: (i) the longitudinal pressure profile $p_0(x_*, y_*)$ (recall that $x_* = x$ and $y_* = y$); (ii) the bulk concentration profile $\tilde{c}(x_*, y_*)$, and (iii) the bulk potential profile $\psi(x_*, y_*, 0)$. For other details, one may refer to §5.1 of the article. The 3D simulations have been carried out in the commercially available finite-element based software COMSOL Multiphysics 5.3, by solving Eq. (3.4), subject to (3.5) and (3.6) in the article. The rendering of the 3D geometry in COMSOL has been illustrated in figure S4(a). This geometry has been constructed using Integrated Computer Engineering and Manufacturing (ICEM) 18.1, which is also a commercially available software.

The choices of solver, tolerance and meshing remain very similar to what was discussed in §S4 for rough fractures. A representative example of the three-dimensional unstructured mesh for the test geometry is depicted in figure S4(b). The total number of computational cells were chosen as 93980, 108262 and 530851, for $\varepsilon = 0.1,\ 0.2$ and 0.3 respectively and $R = 0.1$. We found that further refining the mesh did not affect the accuracy of the simulations. The same workstation as mentioned in §S4 was used to carry out the simulations, which took approximately 12 to 18 hours in accordance with the values of ε.

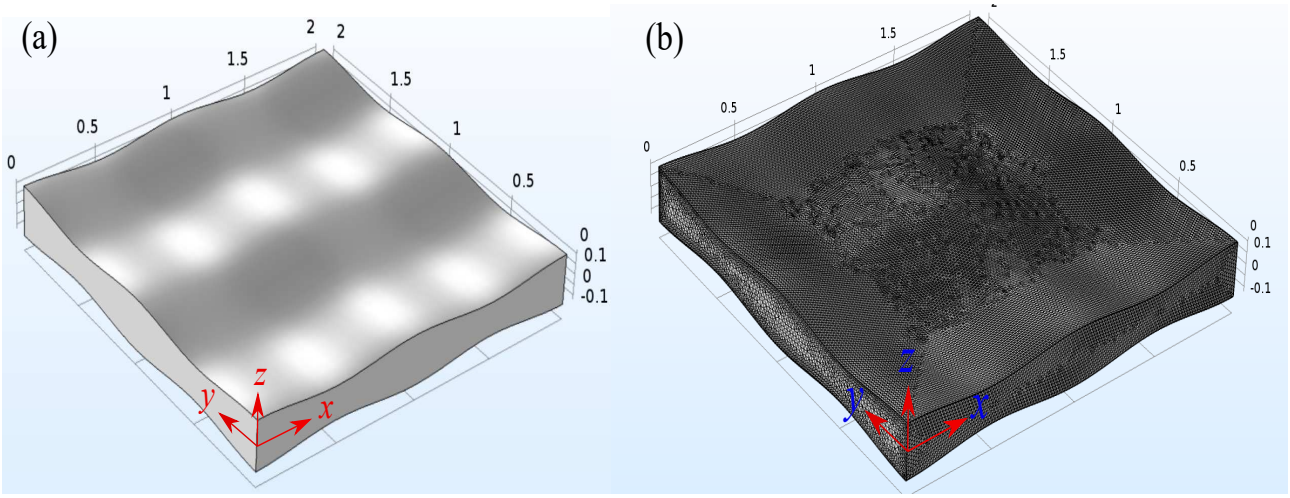

Figure S4: (a) Schematic of the 3D computational domain for the complete numerical simulations. The domain has length $L_x = 2$ and width $L_y = 2$; the top and the bottom surfaces are located respectively at $H_{\mathrm{t},*}(x_*, y_*)$ defined by Eq. (S19) and $H_{\mathrm{b},*}(x_*, y_*) = -H_{\mathrm{t},*}(x_*, y_*)$. We have chosen $\varepsilon = 0.1$ and $R = 0.1$. (b) Mesh created in COMSOL Multiphysics to solve the governing equations.

S5.2 Comparison of results for 3D numerical simulations

Figure S5 shows the comparison between the bulk concentration, induced pressure and the induced potential obtained from the generalized lubrication theory and from the 3D numerical simulations. In subfigures (a), (c) and (d), $\tilde{c}$, $\psi_{\mathrm{ind}} = \psi - \beta x$ and $p_{\mathrm{ind},*} = \varepsilon^{-2}(p_0 - Gx)$ (where $G = \varepsilon^2 G_*$) are respectively plotted as functions of x at $y = 1$, for three choices of $\zeta_0 = 0.5,\ 1$ and 1.2. In subfigures (b), (d) and (f), respectively $\tilde{c}$, ψ and p_* $(= \varepsilon^{-2} p)$ are plotted as functions of y at $x = 0.7$, under identical conditions. The symbols represent results from numerical simulations and the lines exhibit the predictions from the lubrication theory; values of all relevant parameters are mentioned in the caption. Notice that the flow is driven here by a combination of imposed pressure, concentration and potential gradients.

Overall, the trends are very similar to what is observed in figure 3 in the main article. Reasonable agreement between lubrication theory and 3D numerical simulations is noted, while the variations in bulk concentration, potential and pressure follow expected patterns, as governed by the requirement of conservation of salt, current and fluid mass flux.

A more complete picture on the accuracy of the generalized lubrication theory may be obtained by comparing the variations in the quantities of interest along the plane $z = z_* = 0$. Figure S6 compares the contour plots of $\tilde{c}(x, y)$, $\psi_{\mathrm{ind}}(x, y, 0)$ and $p_{\mathrm{ind},*}(x, y, 0)$ as computed from lubrication theory to those of 3D numerical simulations, along $z = 0$. Subfigures (a), (d) and (g) illustrate the results computed using the generalized lubrication theory, whereas subfigures (b), (e) and (h) are plotted based on those obtained from the 3D numerical simulations. The relative errors between the lubrication theory and the numerical simulations are quantified in subfigures (c) for $\tilde{c}$, (f) for ψ_{ind} and (i) for p_{ind}. Values of all relevant parameters are in the caption. Notice that this figure is equivalent to Figure 4 in the main article, but for the test geometry under consideration.

As expected, patterns very similar to those in figure 4 of the article are observed here. The lubrication theory captures the variations in the designated quantities across the plane with reasonable accuracy, with errors less than $O(\varepsilon)$ everywhere. It is interesting to note that in the particular geometry under consideration, the relative errors in concentration and potential lie in the same range as noted for rough fractures in figure 4 of the article, although the relative error in pressure is significantly lower here. The reason may be attributed to the fact that in

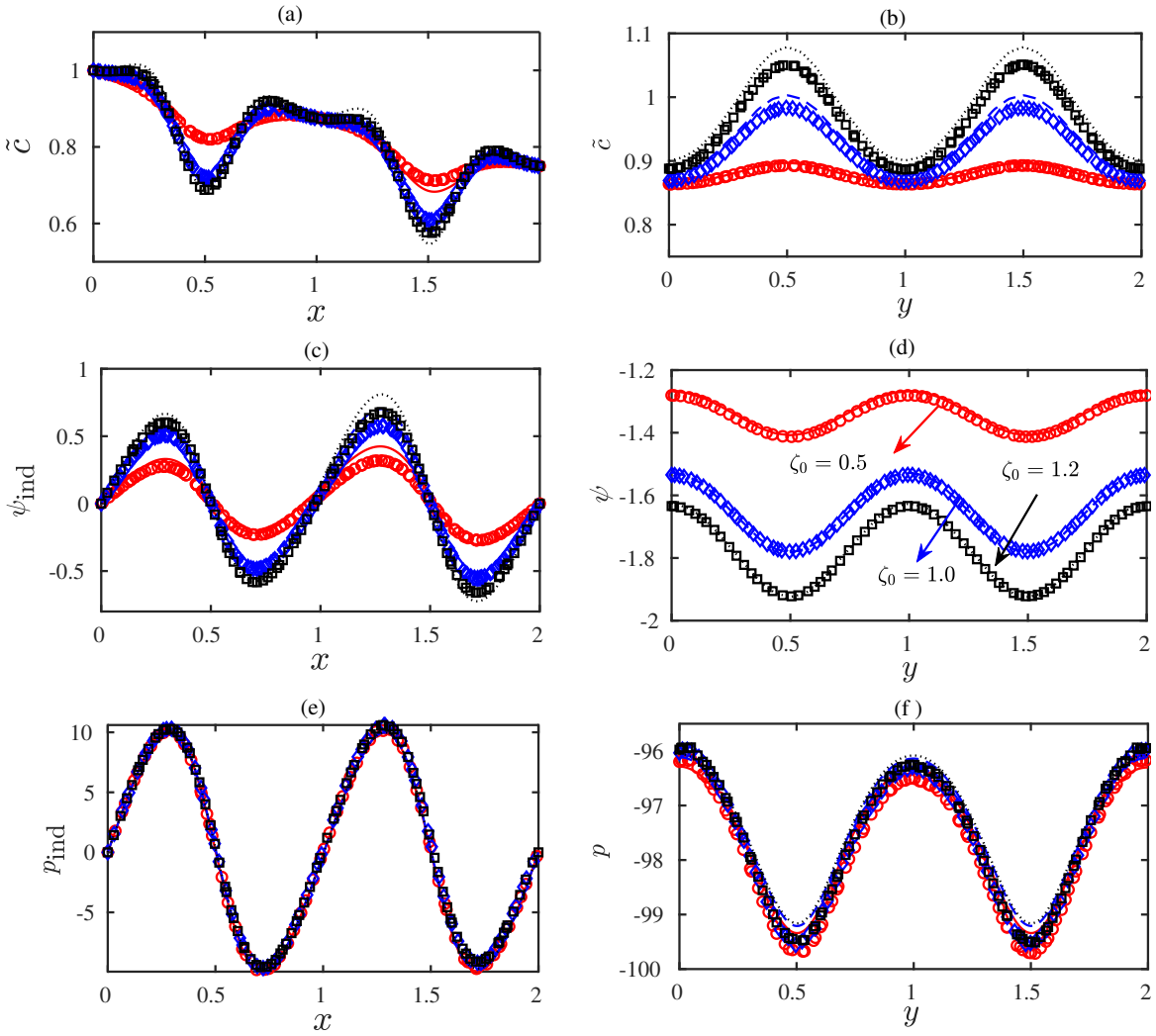

Figure S5: Comparison between the spatial profiles of (a) $\tilde{c}$, (c) $\psi_{\rm ind}$ and (e) $p_{{\rm ind},*}$ as a function of x at $y = y_* = 1$, from the generalized lubrication theory (lines) and the 3D numerical simulations (symbols), for three values of $\zeta_0 = 0.5$ (red circles), 1.0 (blue diamonds) and 1.2 (black squares). (b, d, f) Comparison of the same spatial profiles (for the same quantities) as in (a, c, e), but at $x = 0.7$. The relevant systems parameters are as follows: $\kappa_* = 30$, $\beta = 1.5$, $\alpha = 0.02$, $c_{\rm in} = 1$, $c_{\rm ex} = 0.75$, $p_{\rm in} = 0$, $p_{\rm ex} = -2$ and $Pe = 3$.

the present test geometry, the topology varies more slowly as compared to a rough fracture (in the main article), while the pressure in any flow passage is very sensitive to such topological variations. Hence, the present test geometry fulfills the requirements of the lubrication theory more strongly than a rough synthetic fracture, which results in a relatively more favorable comparison.

As done in Figure 10 in the main article, we also assess the accuracy of the lubrication theory for different values of the length scale ratio $\varepsilon = h_0/l_0$, where l_0 is the wavelength of surface modulations and h_0 is the average aperture in the geometry shown in figure S3. Ideally, the lubrication-based models are only valid for $\varepsilon \ll 1$ [14]. In figure S7, we therefore test the applicability of the lubrication theory by varying the ratio ε from 0.1 to 0.3 and comparing its predictions (lines) with those obtained from the 3D numerical simulations (marker) in the test geometry shown in Fig. S3. Subfigure (a) illustrates the comparison for $\psi_{\rm ind}$, subfig. (b) exhibits the comparison for $\tilde{c}$ and subfig. (c) depicts the comparison for $p_{{\rm ind},*}$, all along the line $y = 1$ (see figure S3); all relevant parameters are given in the figure caption. The trends here are very similar to what was observed in figure 10 of the article: the predictions of the lubrication theory remain reasonably accurate even for $\varepsilon = 0.3$. In fact, the lubrication theory

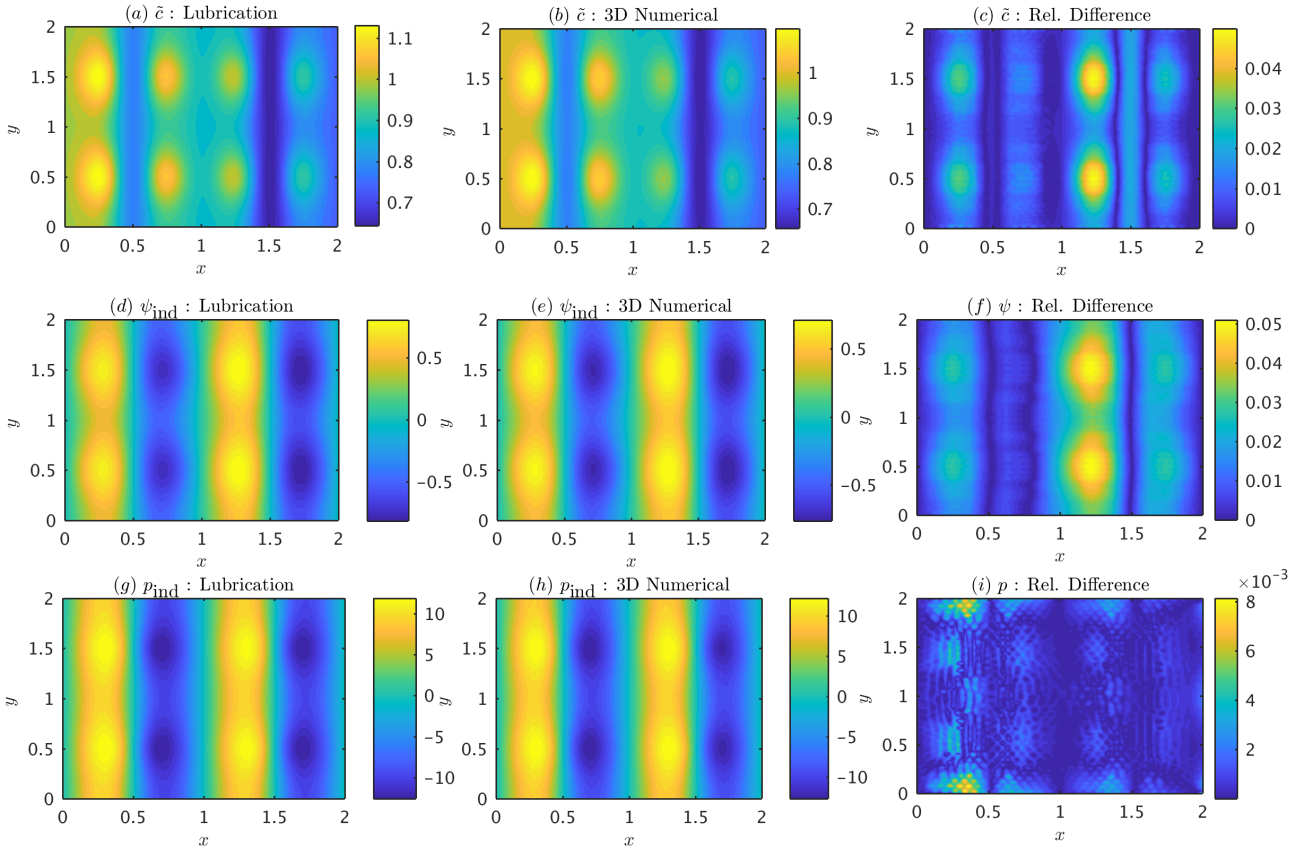

Figure S6: Maps of (a, b) bulk concentration $\tilde{c}$, (d, e) bulk induced potential $\psi_{\rm ind}$, (g, h) induced pressure ($p_{\rm ind} = \varepsilon^2 p_{ind,*}$) along the central plane $z_* = 0$ of the conduit. Figures (a), (d) and (g) exhibit the results obtained from the generalized lubrication theory. Figures (b), (e) and (h) demonstrate the results obtained from the 3D numerical simulations under identical conditions. Figures (c), (f) and (i) respectively illustrate the relative errors between the two approaches in $\tilde{c}$, $\psi_{\rm ind}$ and $p_{\rm ind,*}$. The relevant system parameters are: $\alpha = 0.05$, $\kappa_* = 30$, $\zeta_0 = 1$, $Pe = 3$, $p_{\rm in} = 0$, $p_{\rm ex} = -2$ and $\beta = 1$.

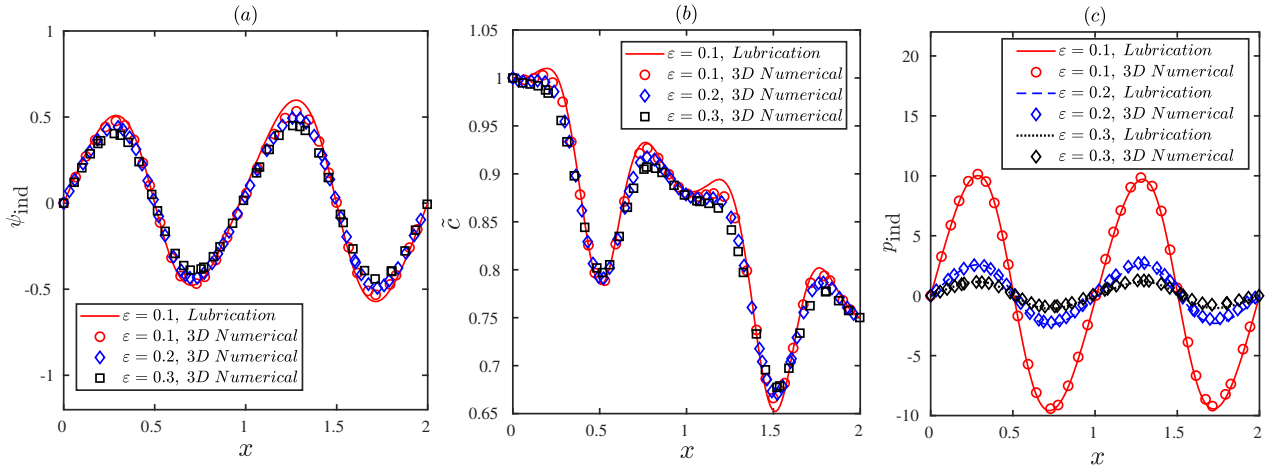

Figure S7: Comparison of the results obtained from the generalized lubrication theory and the 3D numerical simulations for different choices of ε (0.1, 0.2 and 0.3): spatial profiles of (a) $\psi_{\rm ind}$, (b) $\tilde{c}$, and (c) $p_{\rm ind,*}$ as functions of x at $y = 1$. The relevant parameters have the following values: $\beta = 1.0$, $\zeta_0 = 1$, $p_{\rm in} = 0$, $p_{\rm ex} = -2$, $c_{\rm ex} = 0.75$, $\kappa = 30$, $\alpha = 0.05$ and $Pe = 3.0$.

and the 3D numerical simulations exhibit a better match in figure S7, the reason for which may again be attributed to the regular and slowly varying geometry, chosen herein.

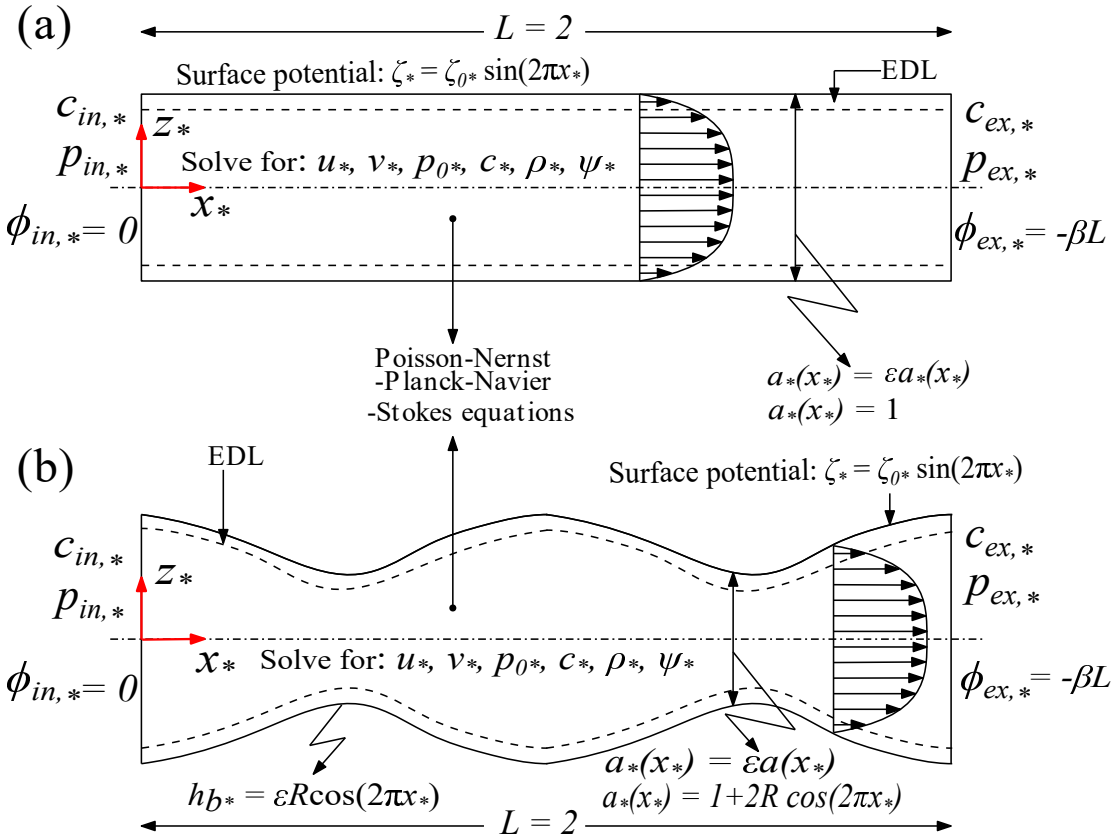

Figure S8: (a) Framework for the comparison for a *parallel plate* fracture, i.e. a fracture of uniform aperture $a_*(x_*) = \varepsilon$; (b) Framework for the comparison for a wavy-wall fracture with aperture field $a_*(x_*) = \varepsilon\{1 + 2R\cos(2\pi x_*)\}$, wherein $h_{\mathrm{t},*}(x_*) = -h_{\mathrm{b},*}(x_*) = \varepsilon R\cos(2\pi x_*)$. The surfaces in both (a) and (b) bear an electrical potential of the form defined by Eq. (S20).

S6 Comparison with 2D numerical simulations of the PNPNS equations

S6.1 The 2D test geometry and the variables compared

In this section, we compare the model based on the generalized lubrication theory (Eq. (S4)) to numerical simulations of the PNPNS equations (Eq. (3.4), subjected to boundary conditions (3.5) in §3 in the main article) in 2D. To this end, two specific geometries have been chosen, (i) a straight channel with uniform aperture $a_*(x_*) = \varepsilon$ (or, $a(x) = 1$) and (ii) a wavy-wall conduit with sinusoidally varying aperture field $a_*(x_*) = \varepsilon\{1 + 2R\cos(2\pi x_*)\}$; please refer to §3 and §4 in the main article for the definition of the various symbols used. The schematics in Figure S8 provides the framework for direct comparison of results between the generalized lubrication theory and the 2D numerical simulations of the PNPNS equations. For this validation, we have considered a symmetric surface potential of the form (as also done in the main article):

$$\zeta_{\mathrm{t}}(x_*) = \zeta_{\mathrm{b}}(x_*) = \zeta(x_*) = \zeta_0 \sin(2\pi x_*) \quad . \tag{S20}$$

We compare the results over a wide range of parameters, which in the process will also provide us with valuable physical insights to the predictions from the generalized lubrication equations.

Much like what is done in the main article, we directly compare the following computed quantities between the two types of numerical simulations: (i) the longitudinal pressure profile $p_0(x_*)$ (recall that $x_* = x$); (ii) the bulk concentration profile $\tilde{c}(x_*)$; (iii) the bulk potential profile $\psi(x_*, 0)$, and (iv) the centerline axial velocity profile $u(x_*, z_* = 0)$. Recall that p_* of the

complete numerical simulations is related to p from the lubrication theory through $p_* = \varepsilon^{-2} p$. We would further clarify that the variables with a "$_*$" subscript represent the dimensionless quantities prior to implementing the rescaled variables using the lubrication theory.

S6.2 The 2D simulation environment

Numerical solutions to the 2D Poisson-Nernst-Planck-Navier-Stokes (PNPNS) equations have been computed using the commercially available finite element based software COMSOL Multiphysics 4.4. We used the MUMPS (Multifrontal Massively Parallel Sparse, see [12, 13]) direct solver with relative tolerance $\gamma = 10^{-4}$ to obtain the numerical solutions. For the straight flow passage (case (a)), l_0 has been chosen as half length of the fracture; for the wavy-wall conduit (case (b)), l_0 is equal to the wavelength of the undulations. Throughout this subsection, we have taken $L = L_x = 2$, which implies $p_{\text{in},*} = 0,\ p_{\text{ex},*} = -2/\varepsilon^2$.

For the simulations in the straight channels, we used rectangular uniform grids. The domain was divided into 400 segments in the axial direction and 60 segments along the vertical (z_*) direction. Therefore, each element in the computational domain had the dimensions $\frac{1}{400} \times \frac{1}{60}$. On the other hand, for the simulations in the wavy-wall channel, we used free triangular mesh to divide the domain into computational cells. The size of the triangular cells essentially depends on the maximum and minimum element size, element size growth rate as well as the maximum allowed iterations to refine the mesh. However, all these control parameters depend on the choices of ε and R. For instance, for $R = 0.2$ and $\varepsilon = 0.05$, the entire domain was divided into 127404 elements. The minimum element size was 4×10^{-4}, the maximum element size was 0.0003; a growth factor of 1.3 and a number of iterations of 15 were used. Refining the mesh to a larger extent did not change the accuracy of the simulations.

For comparison, we have also solved numerically the 2D version of the generalized lubrication equations (S4), using our in-house finite volume method, as described in §4.3 of the main article. For convenience, we still used a three-dimensional domain to solve the said equations, but without any variations along the y-direction. For the ease of numerical computation, we divided the channel plane into 100×4 cells, while at each cross section 500 grid points were chosen to calculate the local flux coefficients.

S6.3 Comparison for straight geometries

We begin with figure S9, which shows the variations in the centerline ($z = 0$) concentration $\tilde{c}$ (subfigure (a)), centerline induced pressure p_{ind} (subfigure (b), see §S5 for definition), centerline induced potential ψ_{ind} (subfigure (c)) and centerline relative velocity $u/\langle u \rangle$ (subfigure (d)) for the flow in a straight channel and for different choices of $\zeta_0 = 0.1$, 0.2, 0.3 and 0.5. The values of the other relevant parameters are given in the figure caption, and $\langle \xi \rangle$ denotes the average of ξ over x. This figure compares the numerical (markers) and analytical (lines) solutions (presented in §S2) of the generalized lubrication theory to the 2D complete numerical simulation results (markers). The analytical solutions have been included to verify the accuracy of the approximate solutions derived in §S2, for low values of ζ_0. The flow here is driven by an imposed pressure and potential gradient along the channel ($p_{\text{ex}} = -2$ and $\beta = 1.5$), and no concentration gradients are imposed, as evident from subfigure S9(a). There are several important points to note from the present figure. First, the solutions derived from the generalized lubrication theory demonstrate reasonably good agreement with the full-scale numerical solutions, therefore underlining the accuracy of the former. Second, we note that for straight channels and low surface potentials, the bulk potential (ϕ) and induced pressure (p_{ind}) exhibit weak to moderate variations with the surface charge magnitude, as can be seen in subfigures S9(b) and (c).

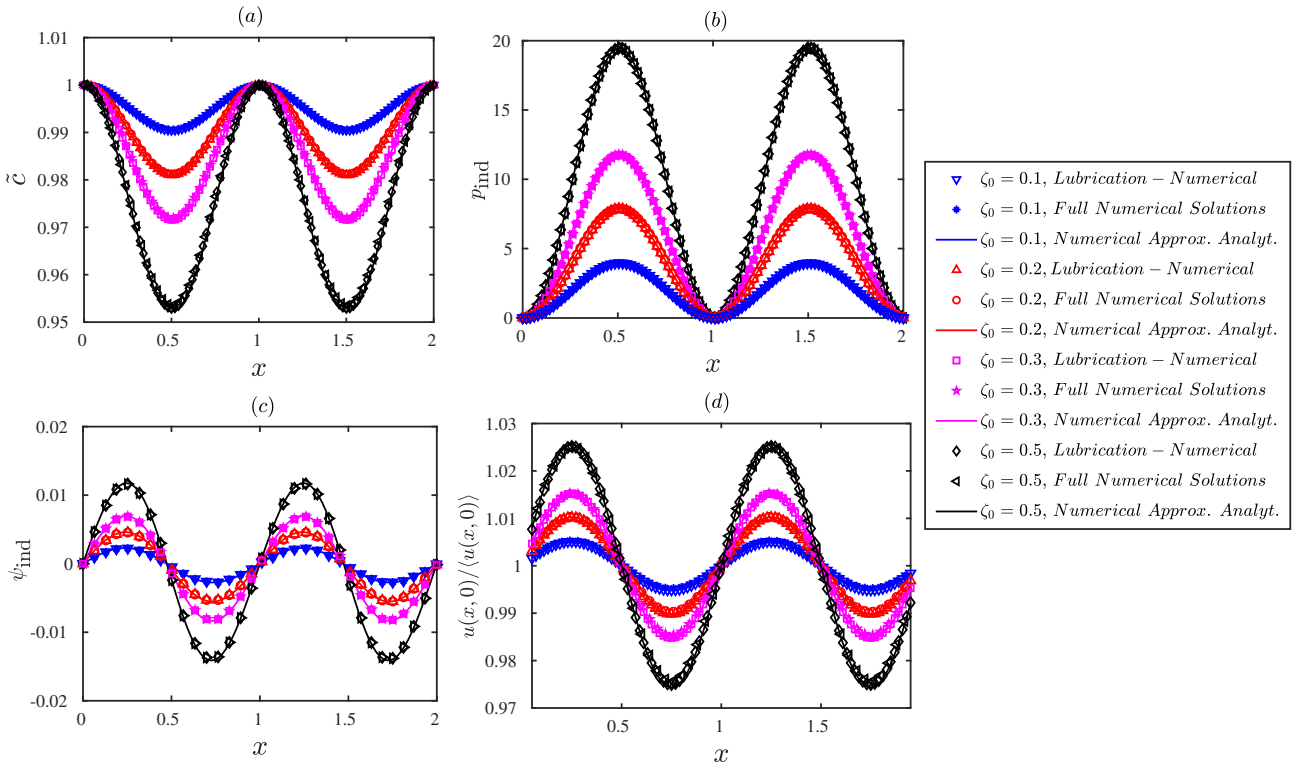

Figure S9: Comparison between the 2D numerical simulations of the PNPNS equations, the generalized lubrication equations and the asymptotic solutions of §S2 for a straight 2D channel and for the following small values of $\zeta_0 = 0.1$, 0.2, 0.3 and 0.5. (a) Variations in the bulk concentration $\tilde{c}$ along the channel; (b) Variation in the induced fluid pressure $p_{\rm ind}$ and (c) Variations in the bulk induced potential $\psi_{\rm ind}$ along the centerline of the channel. (d) Variations in the axial component of the centerline velocity expressed as the ratio $u(x, y = 0)/\langle u(x, 0)\rangle$. The bracket $\langle\rangle$ denotes the average over x. The other relevant parameters have the following values: $\varepsilon = 0.05$, $c_{\rm ex} = 1$, $\kappa = 10$, $\alpha = 0.02$, $\beta = 1.5$, $Pe = 2.0$.

However, the presence of non-uniform surface charge (see Eq. (S20)) results in concentration heterogeneities (i.e., induced spatial variations in bulk salt concentration) in the channel, as evident from subfigure S9(a) and these heterogeneities increase as ζ_0 is increased. The reason for such variations in the bulk concentration has already been discussed in details in relation to Figure 3 in the main article. Finally, from subfigure S9(d) we note that the centerline velocity shows significant variations with x, and that they generally increase as ζ_0 gets larger.

Figure S10 compares the same four quantities as in figure S9 (i.e., (a) $\tilde{c}$, (b) $p_{\rm ind}$, (c) $\psi_{\rm ind}$ and (d) $u(x, 0)/\langle u(x, 0)\rangle$) along the channel axis, for four different values of the externally imposed electric field strength $\beta = 0.5$, 1, 1.5 and 2.0, while the values of the other relevant parameters are mentioned in the caption. In this figure, only the numerical solutions to the generalized lubrication equations (lines) are compared to the complete 2D numerical solutions. We first note that the two solutions show reasonably good agreement for all values of β. The key influence of β is to change the strength of the electro-osmotic component of the flow, although it does not directly alter the ion distribution in the fluid. Nevertheless, we observe from subfigure (a) that increasing β has almost an identical effect on the bulk concentration distribution as that of ζ (see figure S9(a)). Such a behavior can be attributed to the fact that β strongly influences the salt and current flux in the fluid. Larger fluxes, in the presence of a non-uniform surface potential, augments the non-uniformity in the salt and the charge fluxes. Evidence of the said augmentation can be noted from subfigure (d), which shows that the variation in the centerline velocity, with respect to the mean centerline velocity, increases as β becomes larger. This behavior is also very similar to what is observed upon increasing ζ_0 in

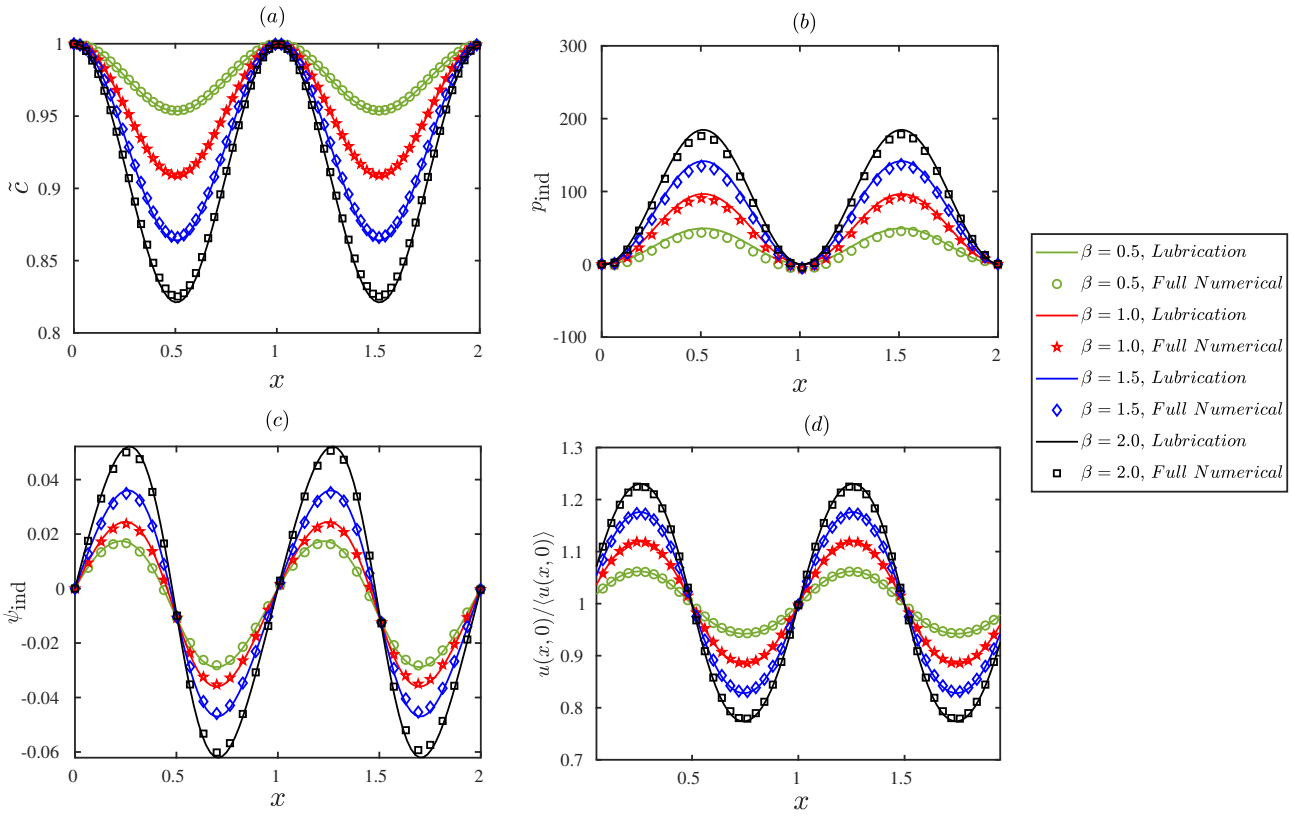

Figure S10: Comparison between the results from the lubrication theory and from the 2D numerical simulations of the PNPNS equations for the following values of β: 0.5, 1.0, 1.5 and 2.0: (a) Spatial variations in bulk concentration $\tilde{c}$ along the channel; (b) Spatial variations in relative induced fluid pressure p_{ind}; (c) Spatial variations in the bulk potential ψ_{ind} along the centerline of the channel and (d) Spatial variations in the axial component of the velocity, expressed as the ratio $u(x, y = 0)/\langle u(x, 0)\rangle$. The other relevant parameters have the following values: $\varepsilon = 0.05$, $c_{\mathrm{ex}} = 1$, $\kappa = 10$, $\alpha = 0.05$, $\zeta_0 = 1.5$, $Pe = 3.0$.

fig. S9. Therefore, an increase in β (i.e., the applied field strength) naturally leads to stronger concentration polarization, occurring due to the constraint of salt mass conservation along the channel. Subfigure S10(a) shows that for $\beta = 2$, the bulk concentration drops almost by 20% as compared to that of an electroneutral solution. Such a large variation also results from choosing a larger ζ value: $\zeta_0 = 1.5$ for the present figure. Finally, the induced pressure p_{ind} also undergoes variations along the channel that are stronger when β is larger. Stronger pressure variations can again be directly linked to non-uniform velocities caused by larger chosen values of β and ζ_0, as evident from subfigure S9(d). Axial non-uniformity in the velocity causes the pressure in the fluid to readjust so that the total volume flux as well as the momentum are conserved.

S6.4 Comparison for undulated geometries

Figure S11 displays the spatial variations in the concentration, centreline pressure profile, electrical potential and centerline velocity in a wavy-walled channel (refer to Fig. S8(b)) subject to an imposed concentration difference of $\Delta\tilde{c} = 0.2$ (here $c_{ex} = 0.8$) and different values of the Péclet number ($Pe = 1$, 5, 10 and 20). The numerical solutions to the complete first principle equations are shown as markers and they exhibit reasonably good agreement with the solutions to the generalized lubrication equations, which are shown as lines. The influence of the imposed concentration gradient is most prominent in the bulk concentration field, as depicted in subfigure S11(a). Notice that the bulk concentration does not vary linearly, with undulations

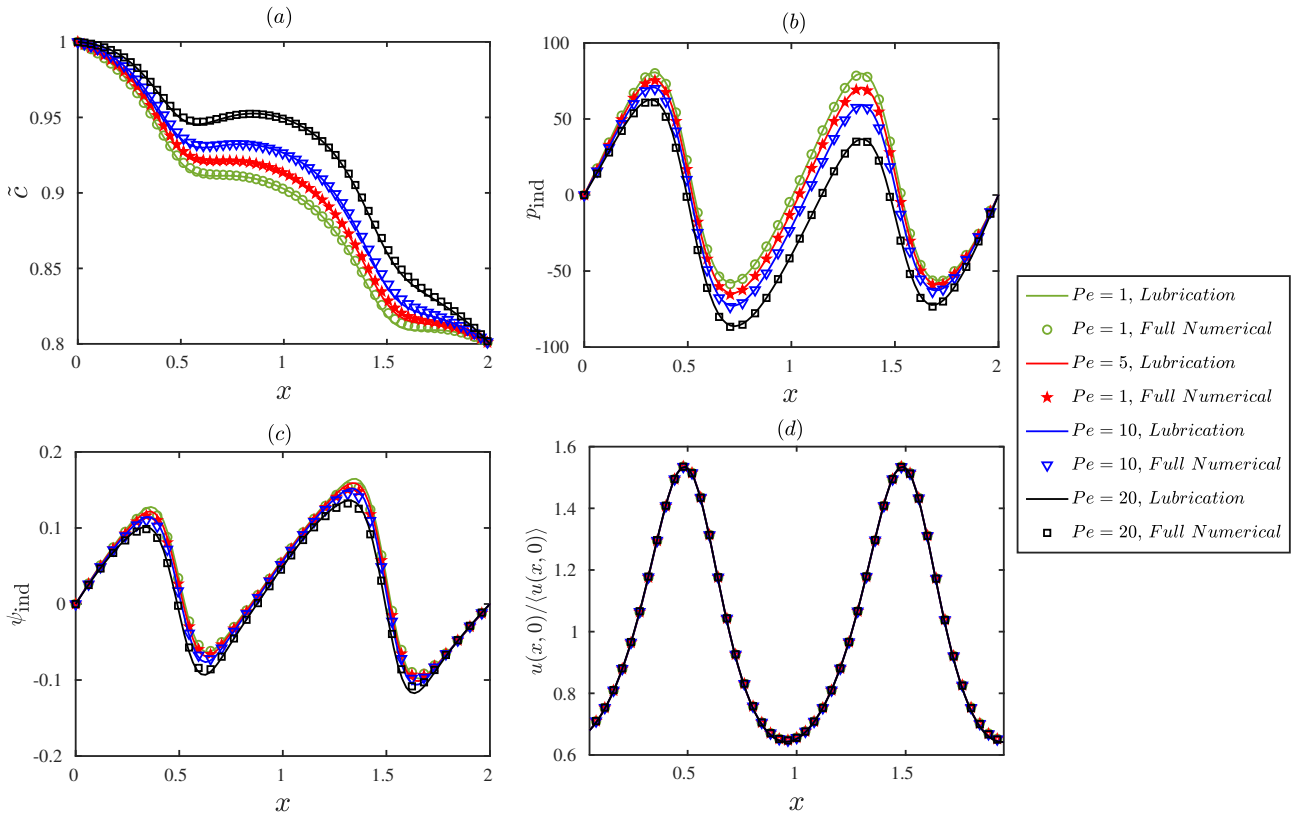

Figure S11: Comparison of results for a wavy channel (Fig. S8(b)) for following values of the Péclet number: $Pe = 1$, 5, 10 and 20. (a) Spatial variations in bulk concentration $\tilde{c}$ along the channel; (b) Spatial variations in relative fluid pressure p_{ind}; (c) Spatial variation in the bulk potential ψ_{ind} along the centerline of the channel and (d) Spatial variation in the axial component of the centerline velocity expressed as the ratio $u(x, z = 0)/\langle u(x, 0)\rangle$. The other relevant parameters have the following values: $\varepsilon = 0.05$, $R = 0.2$, $c_{\mathrm{ex}} = 0.8$, $\kappa = 20$, $\alpha = 0.02$, $\beta = 1$, $\zeta_0 = 1.0$.

owing to the presence of the non-uniform surface potential. Subfigure S11(b) demonstrates the variations in induced pressure (p_{ind}) along the channel. We note that despite the flow occurring along the positive x-direction, the pressure attains the highest value approximately a quarter of the way inside the channel, rather than at the inlet. This is due to the non-uniform influence of the electrical body forces acting in on the fluid, which alter the local pressure so as to conserve the volumetric flow rate (a requirement of the fluid's incompressibility). Another interesting aspect can be found in subfigures S11(a)-(c), where $\tilde{c}$, $\psi+\mathrm{ind}$ and p_{ind} profiles show a considerable amount of asymmetry, especially for $Pe = 10$ and 20, as compared to the previous figures. In all of the previous figures (in §S6), p_{ind}, ψ_{ind} and $\tilde{c}$ profiles are symmetric about the mid-point of the channel. This pattern is clearly broken here at higher Péclet values. Such a behavior can be explained by recalling that Pe essentially denotes the strength of the advection of ions as compared to molecular diffusion. A larger Pe would therefore indicate larger axial advection. Since axial advection tends to drive the ions in the positive x-direction, this naturally creates an asymmetry in the concentration distribution of the salt in the channel. For lower values of Pe the asymmetry is not sufficiently strong to significantly impact the spatial distribution of salt concentrations and pressures; however, it becomes increasingly prominent as Pe gets larger, as evident from subfigures S11(a) - (c). Note however that the absolute dependence of the bulk potential on the advection strength (Pe) is far weaker, as evidenced by panel (c).

We end our discussions with figure S12, which demonstrates the comparative spatial variations of (a) $\tilde{c}$, (b) p_{ind}, (c) ψ_{ind} and (d) $u(x, 0)/\langle u(x, 0)\rangle$) in a wavy-wall geometry with an imposed concentration difference of $\Delta\tilde{c} = 0.2$ for different choices of ζ_0: 0.3, 1 and 2 (the values

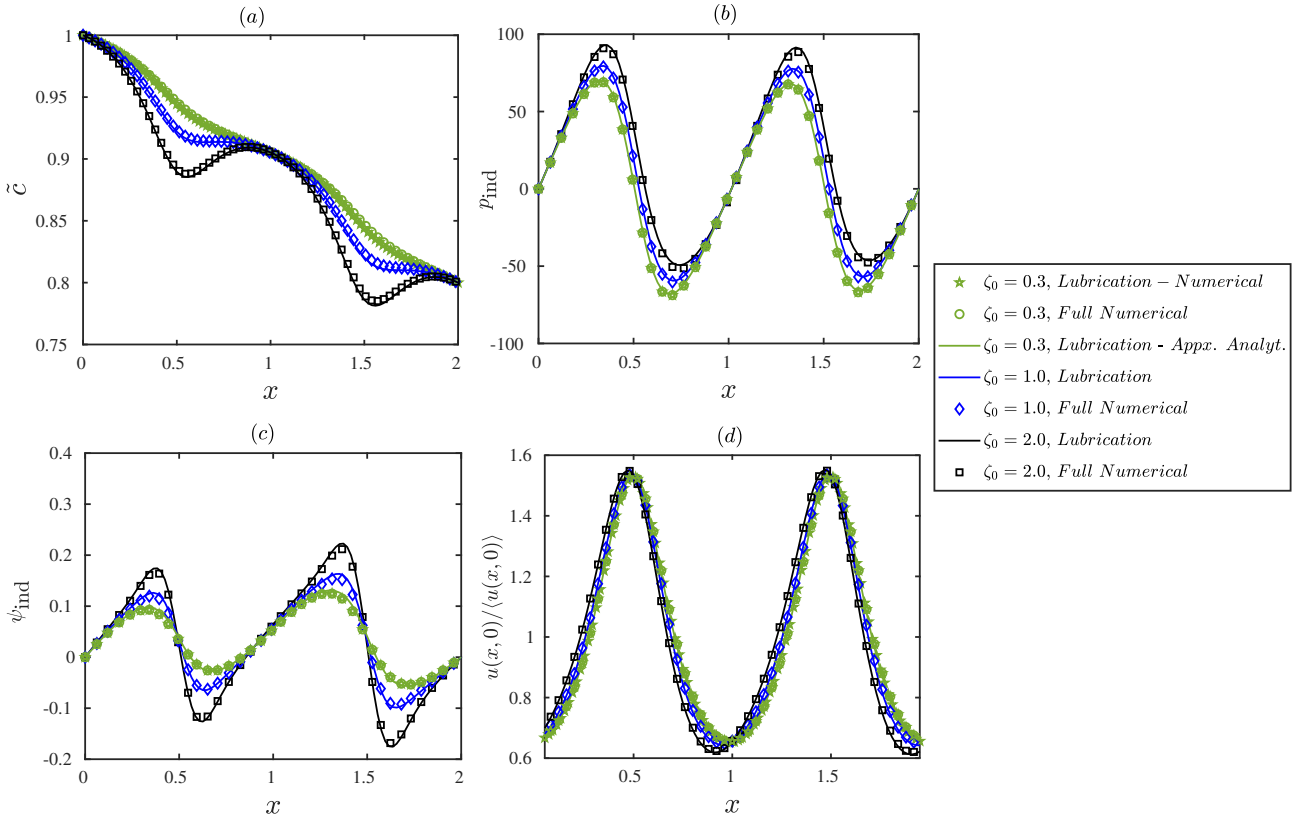

Figure S12: Comparison of results for a wavy-wall channel and for ζ_0 values of 0.3, 1.0 and 2.0 (line for $\zeta_0 = 1$ and 2, marker for $\zeta_0 = 0.3$). The approximate analytical solutions of §S2 are also plotted (green line) for comparison in the case $\zeta_0 = 0.3$. (a) Variations in bulk concentration $\tilde{c}$ along the channel; (b) Spatial variations in relative fluid pressure p_{ind}; (c) Spatial variations in the bulk potential ψ_{ind} along the centerline of the channel and (d) Spatial variations in the axial component of the centerline velocity expressed as the ratio $u(x, y = 0)/\langle u(x, 0)\rangle$. The other relevant parameters have the following values: $\varepsilon = 0.05$, $R = 0.2$, $c_{\mathrm{ex}} = 0.8$, $\kappa = 20$, $\alpha = 0.02$, $\beta = 1$, $Pe = 2.0$.

of other relevant parameters are those mentioned in the caption). The approximate analytical solutions derived in §S2 are also plotted for $\zeta_0 = 0.3$. We first note that the predictions from the lubrication-based model show reasonably good agreement with the full numerical solutions. Overall, similar trends as observed in Figures S9 and S11 are also noted here. Significant undulations in $\tilde{c}$, ψ_{ind} and p_{ind} are observed, while the centerline velocity show very little variations (see subfigure S12(d)) with ζ_0. In fact the variations in the centerline velocity are mostly caused by the non-uniform channel height. As expected, the amplitudes of the fluctuations are larger for larger values of ζ_0, in agreement with figure S9.

References

[1] S. Ghosal. Lubrication theory for electro-osmotic flow in a microfluidic channel of slowly varying cross-section and wall charge. *J. Fluid Mech.*, 459:103–128, 2002.

[2] D. A. Saville. Electrokinetic effects with small particles. *Annu. Rev. Fluid Mech.*, 9(1): 321–337, 1977.

[3] M. S. Kilic, M. Z. Bazant, and A. Ajdari. Steric effects in the dynamics of electrolytes at large applied voltages. ii. modified poisson-nernst-planck equations. *Phys. Rev. E*, 75(2): 021503, 2007.

[4] M. Z. Bazant, M. S. Kilic, B. D. Storey, and A. Ajdari. Towards an understanding of induced-charge electrokinetics at large applied voltages in concentrated solutions. *Adv. Colloid Interf. Sci.*, 152(1-2):48–88, 2009.

[5] O. Schnitzer and E. Yariv. Strong-field electrophoresis. *J. Fluid Mech.*, 701:333–351, 2012.

[6] Uddipta Ghosh, Kaustav Chaudhury, and Suman Chakraborty. Electroosmosis over non-uniformly charged surfaces: modified smoluchowski slip velocity for second-order fluids. *Journal of Fluid Mechanics*, 809:664–690, 2016.

[7] U. Ghosh, S. Mandal, and S. Chakraborty. Electroosmosis over charge-modulated surfaces with finite electrical double layer thicknesses: Asymptotic and numerical investigations. *Phys. Rev. Fluids*, 2(6):064203, 2017.

[8] A. Ajdari. Electro-osmosis on inhomogeneously charged surfaces. *Phys. Rev. Lett.*, 75(4): 755, 1995.

[9] Hiroyuki Ohshima. *Theory of colloid and interfacial electric phenomena*, volume 12. Elsevier, 2006.

[10] S. S Bahga, O. I Vinogradova, and M. Z. Bazant. Anisotropic electro-osmotic flow over super-hydrophobic surfaces. *J. Fluid Mech.*, 644:245–255, 2010.

[11] A. S Khair and T. M. Squires. Fundamental aspects of concentration polarization arising from nonuniform electrokinetic transport. *Phys. Fluids*, 20(8):087102, 2008.

[12] S. Operto, J. Virieux, P. Amestoy, J.-Y. L'Excellent, L. Giraud, and H. B. H. Ali. 3d finite-difference frequency-domain modeling of visco-acoustic wave propagation using a massively parallel direct solver: A feasibility study. *Geophysics*, 72(5):SM195–SM211, 2007.

[13] M. Paszyński, D. Pardo, and A. Paszyńska. Parallel multi-frontal solver for p adaptive finite element modeling of multi-physics computational problems. *J. Comput. Sci.*, 1(1): 48–54, 2010.

[14] L. Gary Leal. *Advanced transport phenomena: fluid mechanics and convective transport processes*, volume 7. Cambridge University Press, 2007.